(Received 10 March 2025, Accepted 14 May 2025, Scheduled 31 May 2025)

A Novel Coaxial Magnetic Gearbox with a Single Input Shaft and Dual Identical Output Shafts

Ali Hosseini-Fard, Seyed H. Shahalami*, and Esmaeil Fallah Choolabi

Department of Electrical Engineering, University of Guilan, Rasht, Iran

ABSTRACT: This paper presents an innovative magnetic gearbox with a three-rotor coaxial structure capable of providing a single input and dual identical outputs. The low-speed rotor magnets of this gear are flux-focusing, while the high-speed rotors magnets are surface-mounted. The performance of this gear was analyzed using finite element analysis. Initially, the gear with initial dimensions was modeled and simulated in ANSYS/Maxwell software, and the results of static and time-dependent analyses were examined. Subsequently, a parametric study of the gear was conducted to investigate the impact of geometric dimension variations on rotor torques and volumetric torque density. The optimal dimensions for achieving the highest volumetric torque density were then selected. The gear was then simulated with the final dimensions, demonstrating that this multi-rotor design is capable of achieving high torque densities (291.61 Nm/L in this gear). Following this, the proposed magnetic gear was compared with another gear of similar dimensions but with three flux-focusing rotors. Additionally, the slicing method was employed for the high-speed rotors magnets to reduce cogging torque, and it was shown that this method successfully reduces the cogging torque of the gear's rotors.

1. INTRODUCTION

Magnetic gears, a concept dating back over a century, have recently garnered significant attention due to advancements in magnet technology. These gears offer the benefit of non-contact power transmission, eliminating the need for lubrication and reducing maintenance requirements. Additionally, they have inherent overload protection. While the initial concept of magnetic power transmission emerged in the early 1900s [1], practical realization of coaxial magnetic gears was limited by magnet technology until the advent of high-performance rare-earth magnets in recent decades. Since 2001, with the introduction of a new type of coaxial magnetic gear employing these powerful magnets, research in this field has experienced substantial growth [2]. A diverse range of magnetic gear designs have been proposed, including radial-flux [3–7], axial-field [8–10], and cycloidal configurations [11, 12]. Researchers have focused on optimizing the volumetric and mass torque density of these gears [13–15].

Figure 1 [6] shows a flux-focusing magnetic gear. This gear consists of two rotors with alternating north and south poles, producing an axial magnetic flux. A ferromagnetic ring, acting as a modulator, is placed between the rotors. Consider a high-speed rotor with p_1 pole pairs rotating at ω_1 and a low-speed rotor with p_3 pole pairs operating at ω_3, and a middle rotor composed of n_2 steel segments rotating at ω_2. The number of ferromagnetic steel segments in the middle rotor is determined by

$$n_2 = p_1 + p_3 \tag{1}$$

The angular speed relationship among the three rotors can be expressed as [2].

$$\omega_1 = \frac{n_2}{p_1}\omega_2 - \frac{p_3}{p_1}\omega_3 \tag{2}$$

The volumetric torque density of a rotary machine can be evaluated using the torque density metric, which is defined as

$$T_d = \frac{T}{\pi r_o^2 d} \tag{3}$$

where T denotes the peak torque of the low-speed rotor, r_o the outer radius, and d the stack length.

Figure 1(b) [8] illustrates an example of an axial-field magnetic gear with surface-mounted magnets. This type of gear consists of two disk-shaped rotors with alternating north and south poles, generating an axial flux. A ferromagnetic ring, acting as a modulator, is positioned between the two rotors, creating a multi-layer configuration. It is worth noting that Equations (1) to (3) remain applicable to this axial-field magnetic gear configuration as well.

The unique characteristics of magnetic gears make them suitable for various applications such as wind turbines [16], automotive powertrain systems [17], and other industries. Despite the rapid progress in magnetic gear technologies, most existing designs are limited to conventional single-input–single-output configurations. This limitation restricts their adaptability in complex systems requiring synchronized multi-output or multi-input transmissions. In practical applications such as electric vehicles or wind energy systems, having multiple outputs with identical torque and speed can significantly simplify mechanical design and improve system integration. However, the development of magnetic gears with more than two shafts

* Corresponding author: Seyed Hamid Shahalami (shahalami@guilan.ac.ir).

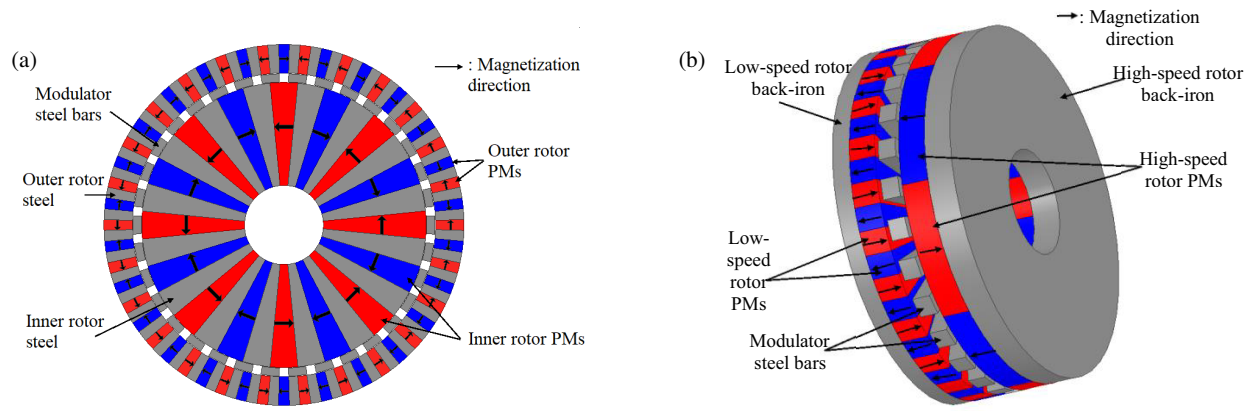

FIGURE 1. (a) A flux-focusing magnetic gear (FFMG) with $p_1 = 8$ pole-pairs on the inner high-speed rotor, $n_2 = 34$ steel poles on the cage rotor and $p_3 = 26$ pole-pairs [6]. (b) An axial-field magnetic gear with $p_1 = 4$ pole-pairs on the high-speed rotor, $n_2 = 27$ ferromagnetic pole-pieces on the modulator and $p_3 = 23$ pole-pairs [8].

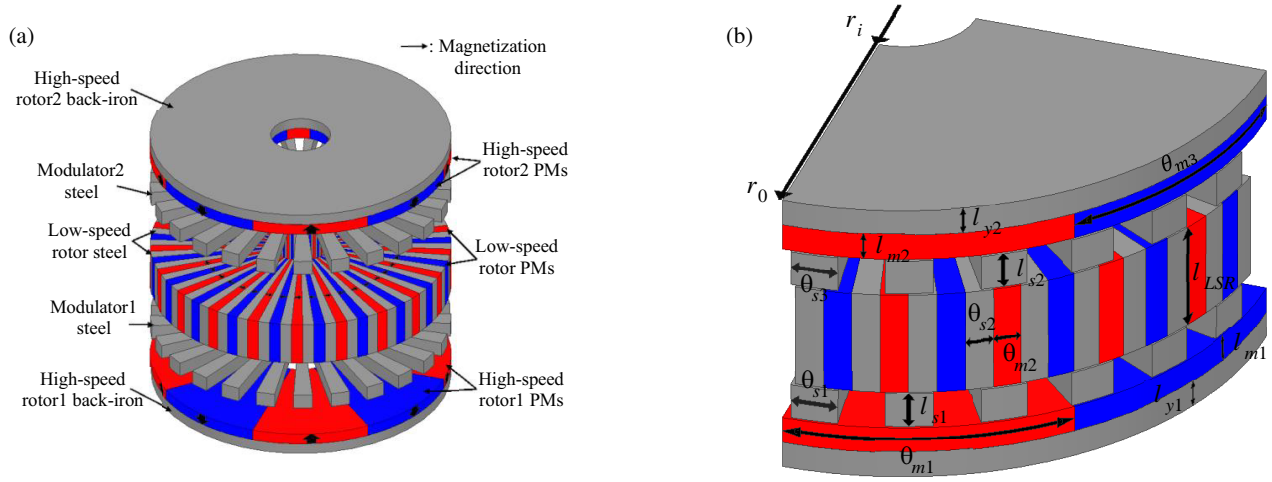

FIGURE 2. The proposed single-input dual-output magnetic gearbox. (a) Exploded view. (b) The geometric parameters.

while maintaining performance symmetry remains largely unexplored.

To address this gap, this study introduces a novel magnetic gear architecture featuring one low-speed input/output shaft and two identical high-speed output/input shafts. Unlike traditional designs, this configuration enables simultaneous transmission of equal torque and speed to two separate shafts. The proposed structure uniquely combines flux-focusing and surface-mounted rotor technologies to leverage the advantages of both, aiming to enhance torque density while maintaining structural simplicity. Furthermore, a slicing technique is employed to reduce torque ripple, which is a critical performance parameter in high-precision applications.

Section 2 of this paper introduces and describes the proposed magnetic gear. The evaluation of this system using finite element analysis, the investigation of the impact of geometric dimension variations on torque and volumetric torque density, and the comparison with another model of the same dimensions and application are performed in Section 3. Section 4 focuses on reducing torque ripple using the slicing method. Section 5 presents the conclusions.

2. A SINGLE-INPUT DUAL-OUTPUT MAGNETIC GEAR

A schematic diagram and exploded view of the proposed coaxial single-input, dual-output magnetic gear are presented in Fig. 2(a). The low-speed rotor (LSR) utilizes azimuthally magnetized magnets, forcing axial flux through the steel poles, while the high-speed rotor1 (HSR1) and high-speed rotor2 (HSR2) magnets are surface-mounted and axially magnetized on the steel yokes. Fig. 2(b) illustrates the geometric parameters of this magnetic gearbox. Additionally, the values of the fixed geometric parameters of this magnetic gear (MG) and its material properties are listed in Table 1. Table 2 presents the sweep parameters and their initial and final values. The initial geometric parameters were chosen based on commonly used dimensions in existing magnetic gear literature to form a feasible baseline for further analysis. Furthermore, a pole combination of $p_1 = p_3 = 4$, $p_2 = 21$, and $n_{C1} = n_{C2} = 25$ was selected to ensure a non-integer gear ratio for reducing the torque ripple [16]. The LSR topology was chosen to be flux-focusing to enable the multi-rotor structure of this gearbox. Furthermore, to achieve a higher volumetric torque density (VTD), the LSR

TABLE 1. Fixed geometric parameters and material properties.

	Description	Value	Unit
High-speed rotors 1	Pole-pairs, p_1	4	-
	Magnet pole span, θ_{m1}	45	degree
	Airgap, g	0.5	mm
Modulator 1	Steel poles, n_{C1}	25	-
	Airgap, g	0.5	mm
Low-speed rotor	Pole-pairs, p_2	21	-
	Steel pole span, θ_{s2}	4.28	degree
	Airgap, g	0.5	mm
Modulator 2	Steel poles, n_{C2}	25	-
	Airgap, g	0.5	mm
High-speed rotors 2	Pole-pairs, p_3	4	-
	Magnet pole span, θ_{m3}	45	degree
	Airgap, g	0.5	mm
Magnet Material (NdFeB 30)	Remanence, B_r	1.2	T
	Relative Permeability, μ_r	1.05	-
Steel material (1018 steel)	steel resistivity	14.2	μΩ-cm

TABLE 2. Initial, final, and geometric sweep parameters.

Description	Initial value	Final value	Sweep values
HSR1, HSR2 back-iron axial lengths, $l_{y_1} = l_{y2}$ [mm]	7.5	8	$[2, 3, \ldots, 20]$
HSR1, HSR2 PMs axial length, $l_{m1} = l_{m2}$ [mm]	7.5	10	$[2, 3, \ldots, 20]$
Modulators 1 and 2 axial lengths, $l_{s1} = l_{s2}$ [mm]	10	7	$[3, 4, \ldots, 10]$
Modulators 1 and 2 steel pole spans, $\theta_{S1} = \theta_{S3}$ [degree]	7.2	7	$[3, 4, \ldots, 10]$
LSR axial length, l_{LSR} [mm]	30	20	$[10, 20, \ldots, 100]$
Inner radius, r_i [mm]	20	30	$[10, 15, \ldots, 55]$
Outer radius, r_0 [mm]	100	150	$[50, 55, \ldots, 170]$

(the rotor with the greater number of pole pairs) was selected as the flux-concentrating rotor [9], as, according to

$$C_{LSR} = \frac{8 l_{LSR} P_2}{\pi \left(r_o + r_i\right)} \tag{4}$$

in a flux-focusing configuration a greater number of pole pairs increases the flux concentration ratio and leads to an increase in the focused flux within the air gaps, consequently increasing the torque. In the above equation, C_{LSR} represents the concentration ratio of LSR, and for this design it is calculated to be 20.05.

Since the objective of this paper is to present a design for a magnetic gear with similar dual outputs/inputs, its high-speed rotors share identical geometric parameters, as its modulators do. Furthermore, in LSR, $\theta_{m2} = \theta_{s2}$ is chosen. It should be noted that the torque and speed of the rotors in the proposed magnetic gearbox are load-dependent. It means that when the gearbox operates as a single-input, dual-output device, the torques on the two outputs will not necessarily be the same, except in the case where the loads placed on the two output rotors are also identical. While the steady-state speeds of the two outputs will be the same, as long as there is no slipping, the torques may differ if there is an angular shift between the two output rotors. Additionally, it is worth noting that during transient events, the speeds of the two outputs may differ. This transient difference in speeds can create a angular shift between the two output rotors.

According to Equation (2), for the two rotors to operate with equal torque and speed, the two modulator rotors must be stationary. Therefore, the gear ratios of LSR to HSR1 and HSR2 are given by

$$G_{r1} = -\frac{p_2}{p_1} \tag{5}$$

$$G_{r2} = -\frac{p_2}{p_3} \tag{6}$$

where G_{r1} and G_{r2} represent the gear ratios of the first and second high-speed rotors, respectively. Since the numbers of pole pairs in these two rotors are equal, their gear ratios are also identical and equal to $5.25:1$.

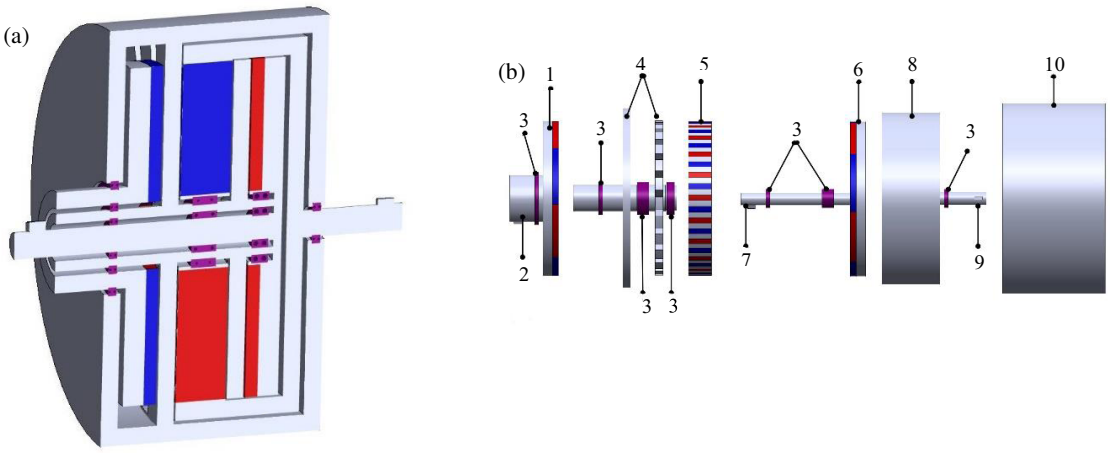

FIGURE 3. Configuration of the proposed magnetic gearbox. (a) Cross-sectional view. (b) Exploded view.

A 3D model of the coaxial multi-rotor magnetic gear was created using SolidWorks software. Fig. 3(a) shows a cross-sectional view of this magnetic gear. The exploded view of this gearbox, along with its various components, is shown and listed in Fig. 3(b) and Table 3.

TABLE 3. Proposed multi-rotor magnetic gearbox parts.

No. of part	Part name	No. of part	Part name
1	HSR1	6	HSR2
2	HSR1 shaft	7	HSR2 shaft
3	Bearings	8	Cap attached to LSR
4	Modulators	9	LSR shaft
5	LSR	10	Gearbox housing

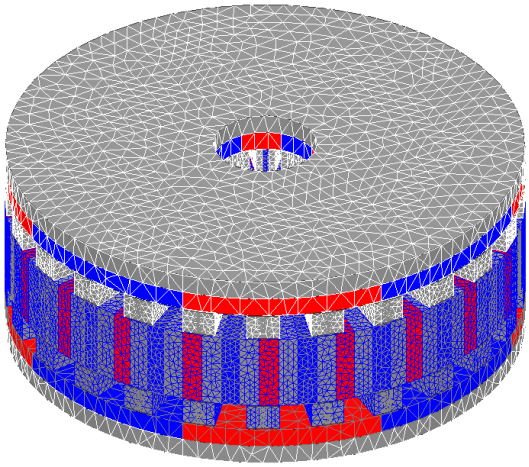

FIGURE 4. Meshing structure of the proposed magnetic gear model.

3. EVALUATION BY FE

3.1. Study of the Proposed MG with Initial Parameters

This magnetic gearbox was analyzed using the finite element (FE) method in ANSYS/Maxwell software, with all analyses performed in 3D. The gearbox was initially simulated with the initial geometric parameters listed in Table 2 under static solver conditions. In this study, the mesh was manually configured in the Maxwell 3D simulation environment to maintain a balance between computational time and simulation accuracy. The mesh size was selected such that it is not too fine which would significantly increase simulation time nor too coarse which could reduce the accuracy of the results. A representative image of the applied mesh is shown in Fig. 4.

The boundary condition applied was the standard insulating type, which is commonly used in 3D electromagnetic simulations. This setting isolates the simulation domain from external fields, ensuring that the calculations are confined to the region of interest.

While a detailed mesh independence verification was not performed due to the limited scope of this study, the simulation settings were chosen in accordance with established practices to ensure reliable and stable results. A full independence verification is considered for future work.

Figure 5 shows the torque of the various rotors as a function of LSR's mechanical angle. The maximum torque of LSR in this simulation was calculated to be 508.31 Nm, and the maximum torques of HSR1 and HSR2 were calculated to be 50.49 Nm and 50.19 Nm, respectively. The maximum torques on the first and second cage rotors were also found to be 302.12 Nm and 307.12 Nm, respectively. Additionally, VTD of the gearbox with these initial parameters was calculated to be 197.31 Nm/L. Note that since the two high-speed rotors are identical and the two modulators also identical, the torque of each of the two rotors is approximately equal. Therefore, in Fig. 5, the blue and red curves (HSR1, HSR2) almost overlap, and the purple and green curves (modulator 1, modulator 2) also overlap.

Figure 6 illustrates the time-dependent behavior of the gearbox's torques with the initial geometric parameters. In this simulation, the modulators were considered stationary, and the LSR was rotated at 200 rpm, while both HSR1 and HSR2 were rotated at 1050 rpm in the opposite direction to the LSR. The average torque of LSR was 324.86 Nm with a torque ripple

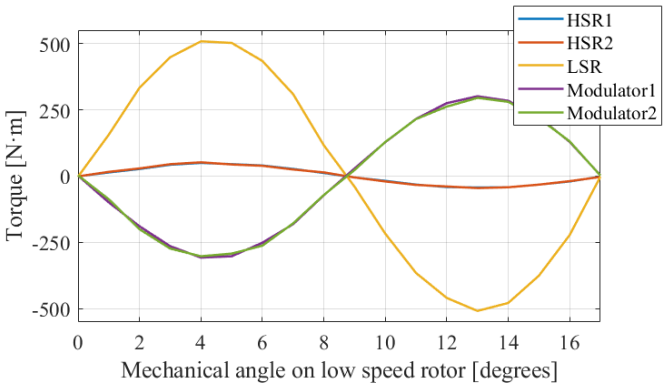

FIGURE 5. Torque on rotors and modulators with initial parameters.

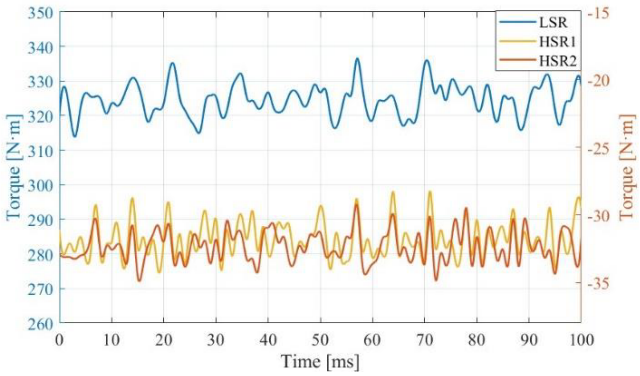

FIGURE 6. Time-domain torque with initial parameters when LSR rotates at 200 rpm, and HSR1 and HSR2 rotate at 1050 rpm.

of 7.69%. Furthermore, the average torques of HSR1 and HSR2 were calculated to be −31.79 Nm and −32.32 Nm, respectively, with torque ripples of 17.52% and 16.27%.

Due to the limited number of simulation steps and mesh resolution in both static and transient analyses, slight differences between the torques of HSR1 and HSR2 were observed, which are within acceptable numerical error. Additionally, the simulation was performed under no-load and lossless conditions, under which the input and output powers should ideally be equal. The observed very slight power mismatch in the transient state can be attributed to numerical approximations and modeling assumptions.

Figure 7 illustrates the magnetic flux density distribution in key components of the proposed axial-flux magnetic gear. In (a), the surface-mounted magnets on the high-speed rotors generate alternating axial flux, with localized saturation near the magnet edges. In (b), the modulators exhibit strong flux concentrations around the ferromagnetic segments, indicating effective field modulation. In (c), the LSR demonstrates a flux-focusing behavior, with dense flux paths concentrated along the pole edges and back iron. These distributions confirm efficient magnetic coupling and validate the gear's flux-focusing and modulation mechanisms.

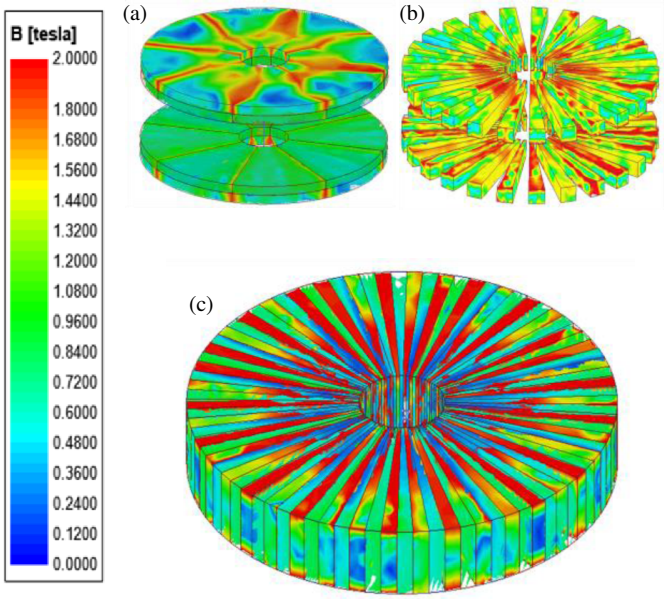

FIGURE 7. Flux density distribution in (a) HSR1 and HSR2, (b) modulators, and (c) LSR.

3.2. Parametric Study of the Proposed MG

A parametric study was conducted to investigate the impact of geometric dimension variations listed in Table 2 on the torques and VTD of the proposed magnetic gearbox. Each parameter listed in Table 2 was optimized independently by varying it while keeping all other parameters fixed at their initial values. Consequently, no physical crossover or overlap occurred in the model during any stage of the parametric analysis. Fig. 8 illustrates the effect of variations in the axial length of the HSR1 magnets on LSR torque and the gearbox VTD, while keeping all other geometric parameters constant. It can be seen that the maximum VTD, which is 204.32 Nm/L, occurs when $l_{m1} = 10$ mm, and the maximum LSR torque, equivalent to 564.5 Nm, is achieved when $l_{m1} = 16$ mm. As shown in Fig. 9, similar to HSR1, the best axial length of HSR2 magnet for maximum VTD (205.21 Nm/L) and maximum torque (565.48 Nm) are 10 mm and 16 mm, respectively.

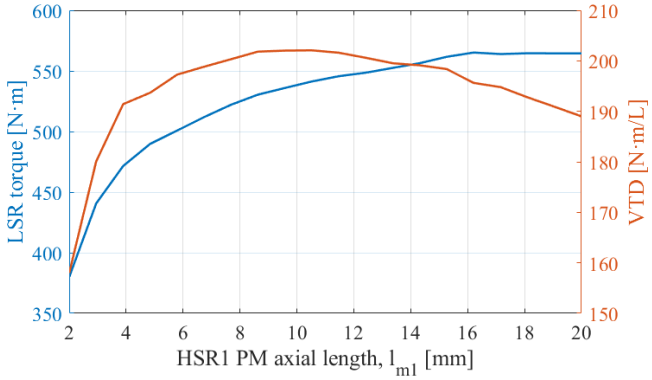

FIGURE 8. Torque and VTD with respect to changes in HSR1 magnets axial length, l_{m1}.

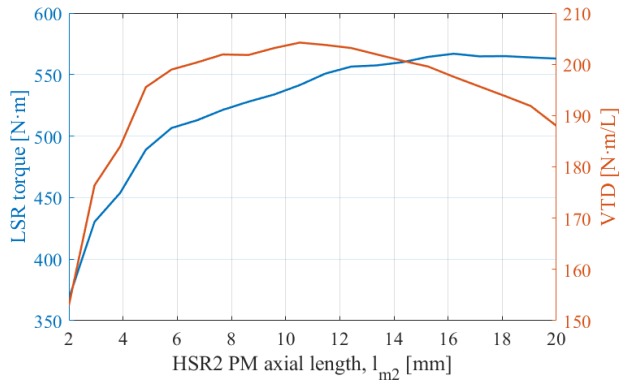

FIGURE 9. Torque and VTD with respect to changes in HSR2 magnets axial length, l_{m2}.

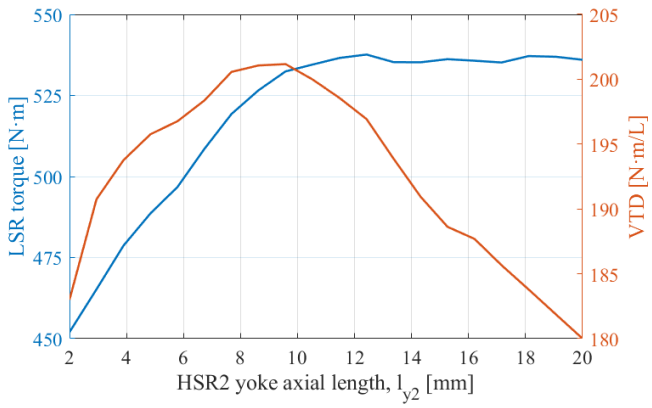

FIGURE 11. Torque and VTD with respect to changes in HSR2 iron-back axial length, l_{y2}.

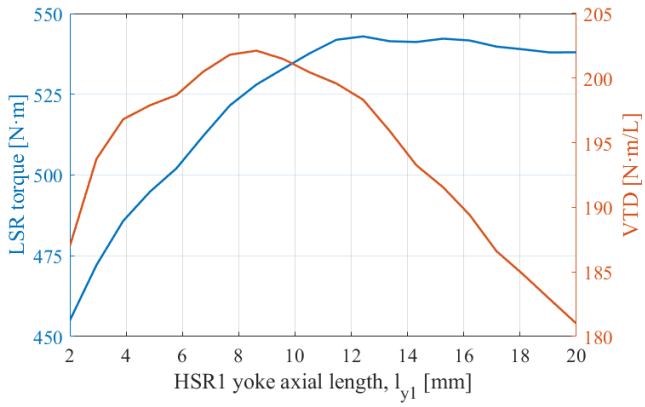

FIGURE 10. Torque and VTD with respect to changes in HSR1 iron-back axial length, l_{y1}.

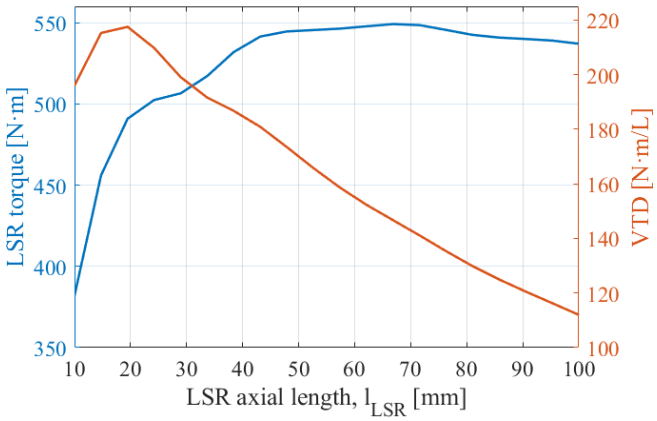

FIGURE 12. Torque and VTD with respect to changes in LSR axial length, l_{LSR}.

The impact of variations in the axial length of the yoke of the first and second high-speed rotors on LSR torque and VTD, while keeping other geometric parameters constant, is shown in Figs. 10 and 11, respectively. As observed, the maximum VTD of the gearbox is achieved when both l_{y_1} and l_{y_2} are 8 mm. This axial length results in a maximum VTD of 202.40 Nm/L for HSR1 and 201.55 Nm/L for HSR2. Furthermore, the optimal value of this parameter for maximizing the LSR torque is 12 mm for both rotors, which yields a maximum torque of 543.21 Nm for HSR1 and 539.44 Nm for HSR2.

Figure 12 illustrates the effect of LSR's axial length on its torque and gearbox VTD. The maximum VTD, with a value of 217.33 Nm/L, is achieved at an axial length of 20 mm, while the maximum LSR torque occurs at an axial length of 70 mm.

Figure 13 demonstrates that the trends in VTD and torque variations with respect to changes in the inner radius follow a similar pattern, as the inner radius does not affect the VTD according to Equation (3). The peak VTD (206.72 Nm/L) and LSR torque (532.54 Nm) are achieved when $r_i = 30$ mm. The appearance of the double peaks in torque and VTD is likely due to nonlinear variations caused by changes in r_i, as observed in simulations within the range of 10 cm to 30 cm. This behavior may result from complex interactions among magnetic fluxes, the geometry of permanent magnets, and other design factors.

As illustrated in Fig. 14, the relationship between the outer radius and the torque is approximately linear and increasing. However, the VTD starts to plateau beyond $r_o = 150$ mm. The maximum torque density of 259.21 Nm/L is achieved at $r_o = 150$ mm, while the torque continues to increase with larger outer radii, reaching 1892.3 Nm at $r_o = 170$ mm. Since the objective of the optimization is to maximize the VTD, an outer radius of 150 mm has been selected for the final optimized model.

Figure 15 examines the effect of variations in the axial length and the bar span of the modulators on VTD, while keeping other parameters constant. The maximum VTD occurs when $l_{s1} = 7$ mm and $l_{s2} = 7$ mm and $\theta_{S1} = 7$ degrees and $\theta_{S3} = 7$ degrees. Selecting these values results in a VTD of 217.57 Nm/L for the first modulator and 214.02 Nm/L for the second modulator.

3.3. Study of Proposed MG with Final Parametes

Following the parametric study of this gearbox, the optimal dimensions of the sweep parameters for achieving maximum VTD were selected. These final geometric parameters are listed in Table 2. Using these dimensions, further static and transient simulations were performed for comparison with the initial model. Fig. 16 illustrates the torque of the rotors and sta-

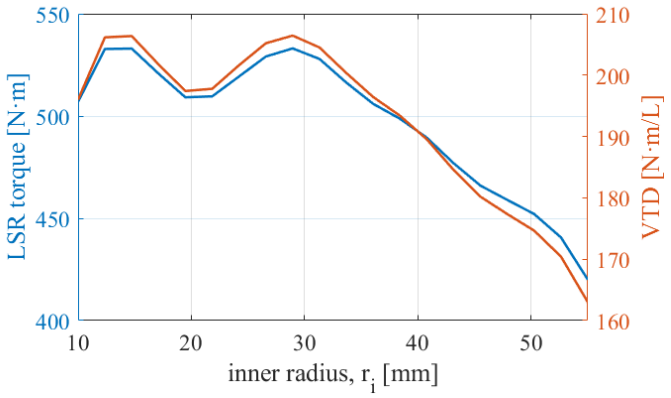

FIGURE 13. Torque and VTD with respect to inner radius, r_i.

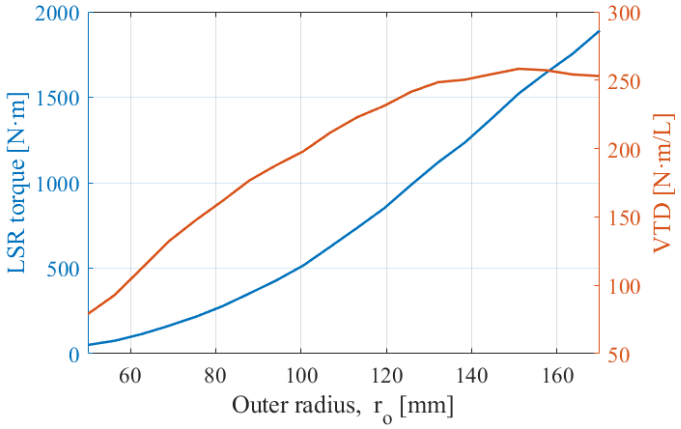

FIGURE 14. Torque and VTD with respect to outer radius, r_o.

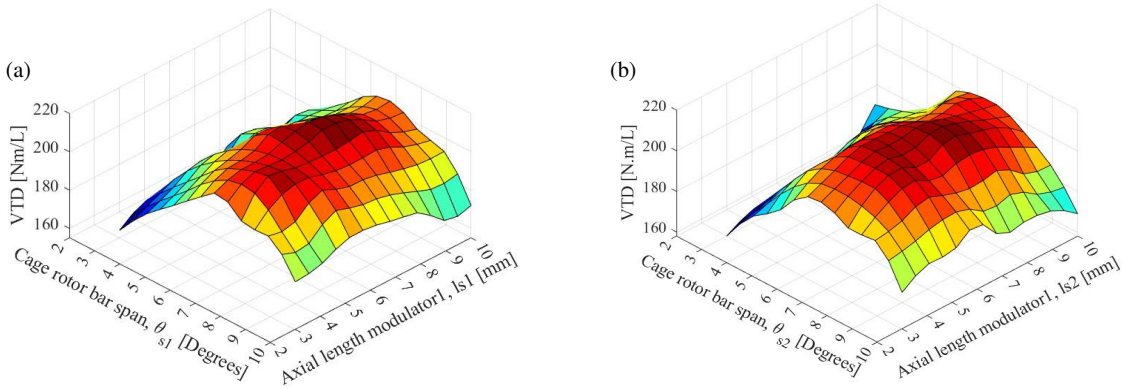

FIGURE 15. The impact of variations in axial length l_{s1}, l_{s2}, and steel pole span θ_{S1}, θ_{S3} on VTD for (a) modulator 1, and (b) modulator 2.

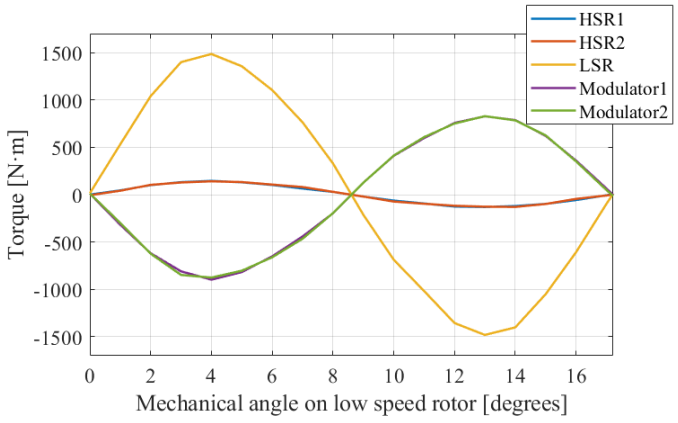

FIGURE 16. Torque on rotors and modulators with final geometric parameters.

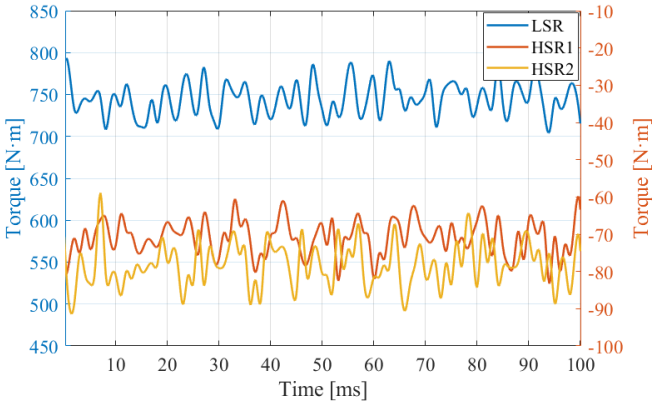

FIGURE 17. Time-domain torque with final geometric parameters when LSR rotates at 200 rpm and HSR1 and HSR2 rotate at 1050 rpm.

tionary modulators as a function of the LSR's mechanical angle. The maximum torque of the LSR is 1484.34 Nm, and the peak torques of HSR1 and HSR2 are 145.17 Nm and 140.82 Nm, respectively. Additionally, the maximum torques of the first and second modulators are 827.06 Nm and 828.22 Nm, respectively. Furthermore, the VTD of this gearbox with these dimensions is 291.61 Nm/L, which is a significant value.

Figure 17 illustrates the rotor torques of this gearbox in a transient analysis. Similar to the simulation with the initial dimensions, LSR rotates at 200 rpm, and HSR1 and HSR2 rotate at 1050 rpm, each in the opposite direction of the LSR. The average torques of LSR, HSR1, and HSR2 were calculated to be 744.33 Nm, −70.91 Nm, and −78.19 Nm, respectively. Furthermore, the torque ripple for LSR is 13.99%, and for HSR1 and HSR2, it is 29.53% and 29.28%, respectively.

It is worth mentioning that, under optimized conditions, the torque of HSR1 becomes slightly greater than that of HSR2, unlike in the initial design where they were nearly equal. This shift may be related to the significant changes introduced by geometry optimization, although a more detailed investigation would be needed to fully explain this behavior. Furthermore, the slight increase in torque ripple after optimization is mainly attributed to the higher torque and torque density achieved through changes in key dimensions and enhanced magnetic flux interactions. Compared to the model with the initial parameters, these dimensions provide significantly larger torques and VTD, but also increase the torque ripple. These results demonstrate the potential of this gearbox to achieve high VTD's.

3.4. Comparison of the Proposed MG with the Same MG but a Different Design

In this subsection, the proposed magnetic gearbox with the initial design parameters is compared with another topology based on a different rotor configuration but the same application. For a fair comparison, the two designs share identical volumetric dimensions, pole pair numbers, and gear ratios. The aim of this comparison is to evaluate the effectiveness of the proposed structure, which uses a hybrid configuration (flux-focusing in LSR and surface-mounted in HSRs), against a fully flux-focusing design where all three rotors are flux-focusing magnetized. This specific topology was selected because, as demonstrated in previous studies such as [9], fully flux-focusing configurations often deliver higher torque transmission in conventional two-rotor magnetic gears. However, this study investigates a more complex structure with three rotors, and the proposed hybrid design achieves superior performance in both torque/VTD and torque ripple reduction. It is important to emphasize that the fully flux-focusing model is not optimized and has the same geometric parameters as the initial design of the proposed gearbox to ensure a fair one-to-one comparison.

Figure 18 illustrates the magnetic gear with two identical output shafts, where all three rotors are flux-focusing magnetized. Fig. 19 shows the static torque of the rotors and modulators of this gearbox as a function of the LSR's mechanical angle. According to the figure, the maximum torques of LSR, HSR1, HSR2, and the first and second modulators are 394.36 Nm, 35.01 Nm, 36.27 Nm, 232.37 Nm, and 231.76 Nm,

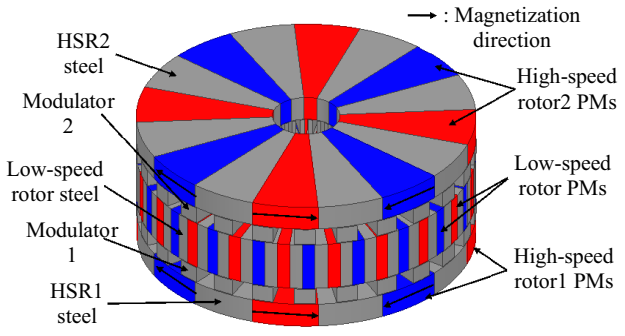

FIGURE 18. A single-input dual-output magnetic gearbox having the three rotors flux-focusing magnetized.

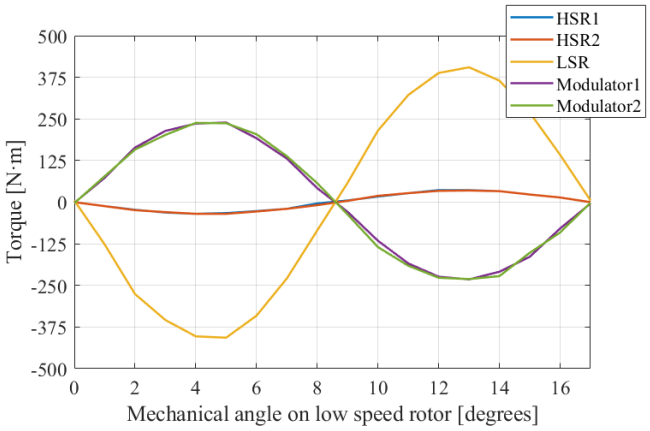

FIGURE 19. Static torque on rotors and modulators.

respectively. The VTD of this gearbox was calculated to be 153.08 Nm/L, which is 22.41% lower than that of the surface-mounted model analyzed in Section 3.1.

Figure 20 illustrates the time-dependent torques of the rotors of this gearbox under the same conditions as the proposed model. The average torques of LSR, HSR1, and HSR2 are 231.77 Nm, -22.77 Nm, and -23.22 Nm, respectively, which are lower than those of the proposed model. Furthermore, the torque ripples of these rotors were calculated to be 11.06%, 18.86%, and 20.52%, respectively, which are higher than the torque ripples of the rotors in the proposed model with the initial geometric dimensions discussed in Subsection 3.1.

4. COGGING TORQUE REDUCTION

4.1. Cogging Torque Minimization Method

In a magnetic gear, cogging torque results from the interaction between the permanent magnets of the rotors and the iron structure of the modulators, and it is equivalent to torque ripple [19]. Zhu and Howe introduced cogging factor [18] while investigating how pole and slot combinations in electrical machines affect cogging torque. This factor can be calculated as

$$C_f = \frac{p * n_c}{LCM\,(p, n_c)} \tag{7}$$

where LCM is the least common multiple, p the number of pole-pairs, and n_c the number of pole-pieces. For the proposed magnetic gearbox, this factor is 1, which is a proper value. However, in the MG with initial parameters, there is still a cogging torque of 7.69%, 17.52%, and 16.27% in LSR, HSR1, and HSR2, respectively.

In this section, the slicing method will be employed to reduce the cogging torque of this gearbox with initial parameters. To reduce cogging torque, the magnetic gear's rotors are segmented into n slices. Each slice is then angularly shifted by a specific angle α. For instance, in Fig. 21 ($n = 3$), the second slice is rotated by α relative to the first and the third by 2α relative to the first. This misalignment ensures that the d-axis of each slice's magnets aligns with pole pieces at distinct positions. Consequently, the overall cogging torque is the vector

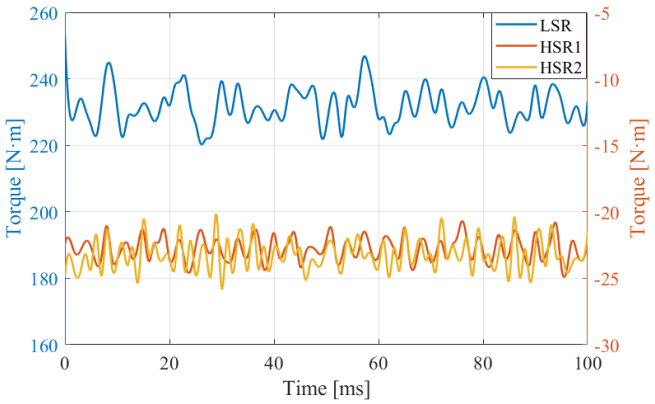

FIGURE 20. Time-domain torque when LSR rotates at 200 rpm and HSR1 and HSR2 rotate at 1050 rpm.

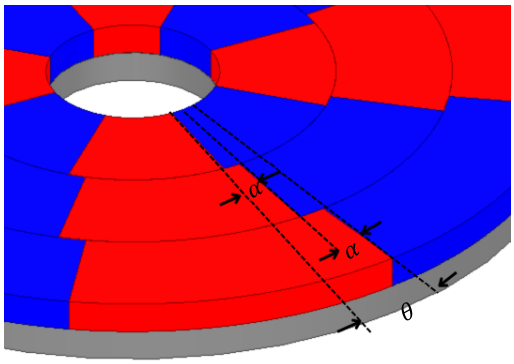

FIGURE 21. HSR1 and HSR2 magnets sliced in three segments.

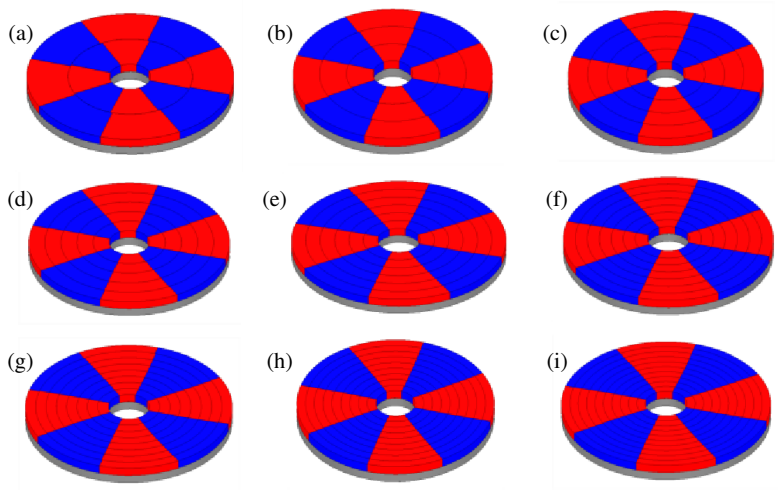

FIGURE 22. Slicing models employed to HSR1 and HSR2 of the proposed magnetic gearbox. (a) $n = 2$. (b) $n = 3$. (c) $n = 4$. (d) $n = 5$. (e) $n = 6$. (f) $n = 7$. (g) $n = 8$. (h) $n = 9$. (i) $n = 10$.

sum of the individual slice torques, leading to a reduced magnitude [20]. The cogging torque period θ in mechanical degree is defined as [21]

$$\theta = \frac{360^\circ}{LCM\,(p, n_C)} \tag{8}$$

according to Equation (8), the cogging torque period for LSR is 0.342°, and for the high-speed rotors, it is 1.8°. Since the value is lower in LSR, it has a smaller impact on the cogging torque than high-speed rotors. Therefore, the slicing method will only be applied to high-speed rotors in this case. For n number of slices, each slice should be rotated by α, where $\alpha = \frac{\theta}{n}, n > 1$.

4.2. Simulations and Results

As illustrated in Fig. 22, different models with different numbers of slices were investigated for this purpose. Each of these models was analyzed respectively using finite element analysis (FEA) with the same time domain. Table 4 lists the values of angular rotation α required for both high-speed rotors in each sliced model, where $n = 1$ indicates the original, unsliced configuration. Fig. 23 provides a comparative analysis of the average torque and cogging torque values between the original and proposed models. As observed in Figs. 23(a) and 23(b), LSR average torque has increased, and its torque ripple has decreased. Although the slicing method was only applied to HSR1 and HSR2, the reduction in cogging torque for LSR is less significant than HSR1 and HSR2. Figs. 23(c) and 23(e), as well as 23(d) and 23(f), demonstrate that this method has a minimal impact on the high-speed rotor torques but successfully reduces their cogging torques.

In order to find the optimal rotor slicing configuration, a factor β was introduced. This factor can be as an objective function

TABLE 4. The value of Slicing angles on the magnets of HSR1 and HSR2.

No. of slices n	α (deg) HSR1, HSR2	No. of slices n	α (deg) HSR1, HSR2
1	-	6	0.3
2	0.9	7	0.25
3	0.6	8	0.22
4	0.45	9	0.2
5	0.36	10	0.18

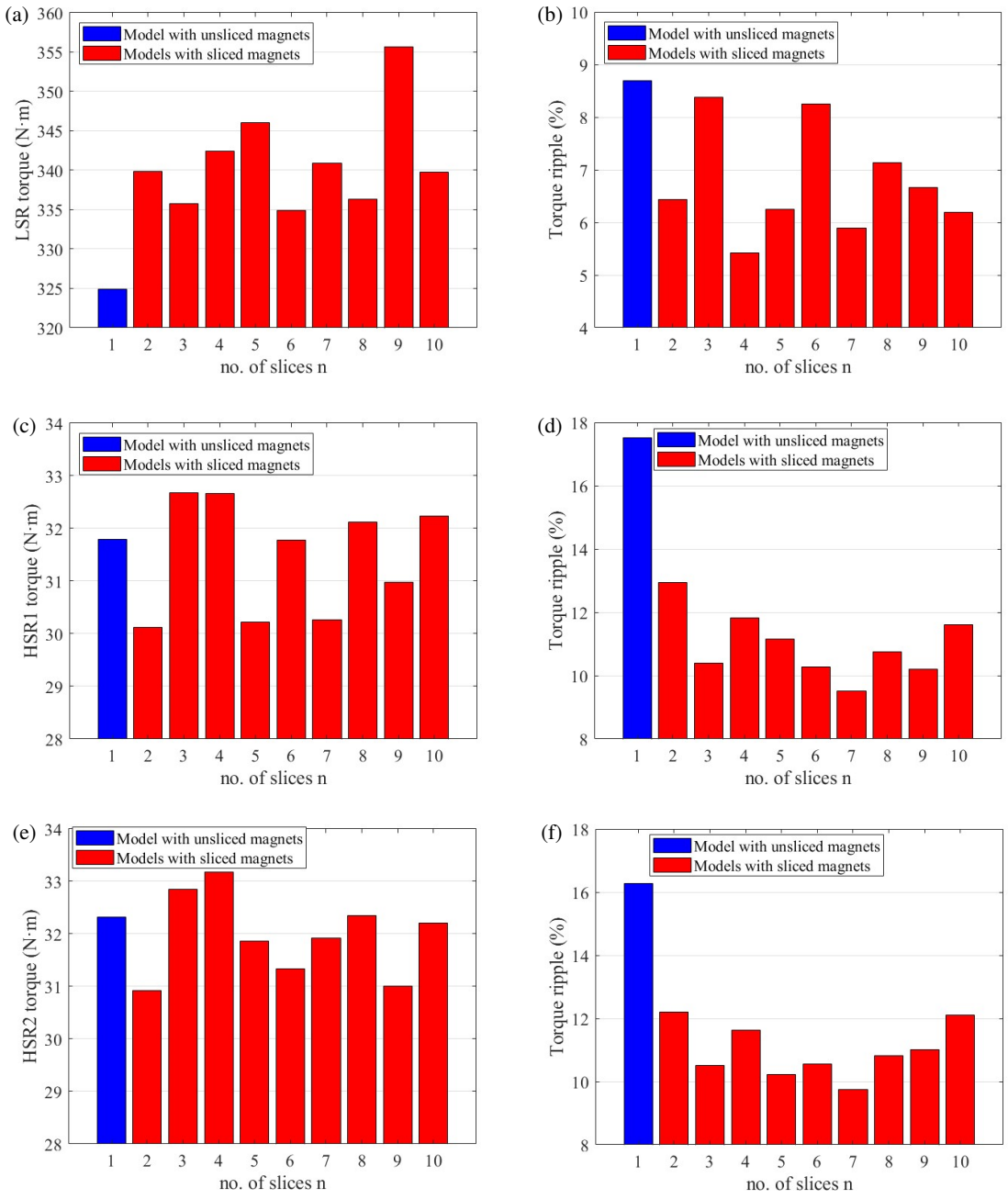

FIGURE 23. Comparison of torque values and torque ripple percentages of all models. (a) LSR torque. (b) LSR torque ripple percentage. (c) HSR1 torque. (d) HSR1 torque ripple percentage. (e) HSR2 torque. (f) HSR2 torque ripple percentage.

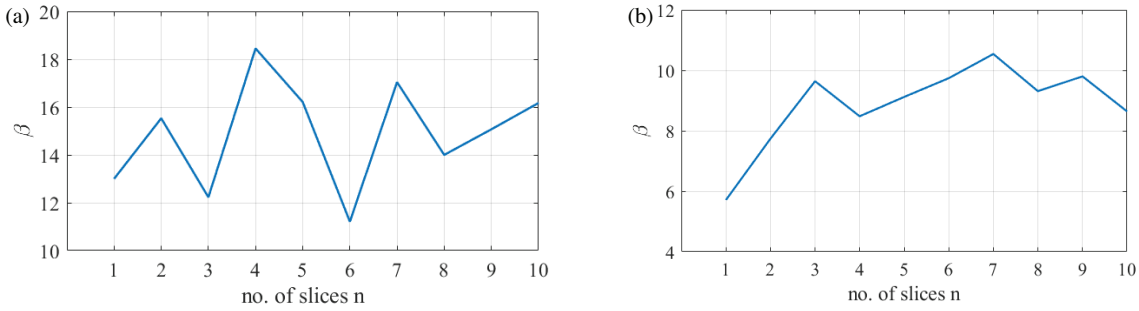

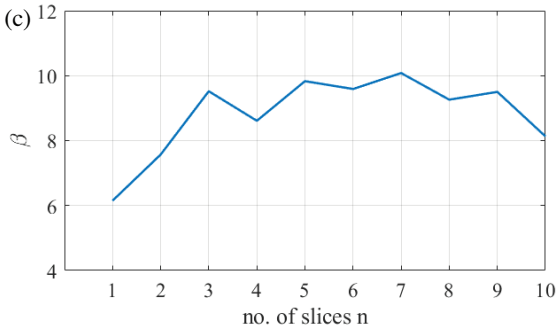

FIGURE 24. Average torque to cogging torque ratio of the (a) LSR, (b) HSR1, and (c) HSR2.

of maximum average torque and minimum cogging torque, and is defined by

$$\beta = \frac{T_{avg}}{T_{cog}} \tag{9}$$

A higher value of β indicates a lower cogging torque. Fig. 24 illustrates the relationship between β and the number of rotor slices n for each of the three rotors. The results demonstrate the effectiveness of the slicing method in enhancing the magnetic gearbox's performance. Specifically, Fig. 24(a) shows an optimal β value at $n = 4$ for LSR, whereas Figs. 24(b) and 24(c) show optimal points at $n = 7$ for HSR1 and HSR2.

5. CONCLUSION

In this paper, a novel coaxial magnetic gear featuring a single input and two identical outputs is introduced and comprehensively analyzed. It is the first time that such a configuration has been proposed, addressing the need for dual-output magnetic transmission in compact systems. The design and analysis were carried out using 3D finite element simulations in ANSYS/Maxwell. Initially, with the preliminary geometric dimensions, the gear exhibited a volumetric torque density (VTD) of 197.31 Nm/L, and the maximum torque of the low-speed rotor reached 508.41 Nm. Following a parametric study and geometric optimization, the final design achieved a significantly enhanced VTD of 291.61 Nm/L, which is remarkably high for a magnetic gear. Based on the transient (time-dependent) simulation, the low-speed rotor generated an average torque of 744.33 Nm with a 13.99% cogging torque, while the two high-speed rotors produced -70.91 Nm and -78.19 Nm average torques, with torque ripples of 29.53% and 29.28%, respectively. The gearbox was also compared with another topology where all three rotors were flux-focusing magnetized, showing that the proposed structure delivered higher torque density and lower torque ripple under identical conditions. Furthermore, rotor slicing was applied to reduce cogging torque, confirming its effectiveness. The proposed magnetic gearbox, due to its high VTD capability, can be utilized in various applications. One of the primary applications can be in wind power generation systems, where the gear can drive two parallel generators from a single turbine, increasing power generation capacity and ensuring continuous operation even if one generator fails, or, it can operate as a dual-input single-output magnetic gear, combining the torque from two sets of wind turbine blades and delivering it to a single generator. Another application is in electric vehicles (EVs), where the gear can distribute power from a single motor to both the front and rear axles, enhancing vehicle stability and energy efficiency. Future research can focus on the fabrication of a prototype model, experimental validation in real-world applications, and dynamic analysis of the gear's behavior under varying conditions such as acceleration, deceleration, and load disturbances.

REFERENCES

[1] Armstrong, C. G., "Power transmitting device," U.S. Patent 687,292,26, 1901.

[2] Atallah, K. and D. Howe, "A novel high-performance magnetic gear," *IEEE Transactions on Magnetics*, Vol. 37, No. 4, 2844–2846, 2001.

[3] Rasmussen, P. O., T. O. Andersen, F. T. Jorgensen, and O. Nielsen, "Development of a high-performance magnetic gear," *IEEE Transactions on Industry Applications*, Vol. 41, No. 3, 764–770, 2005.

[4] Jian, L., K. T. Chau, Y. Gong, J. Z. Jiang, C. Yu, and W. Li, "Comparison of coaxial magnetic gears with different topologies," *IEEE Transactions on Magnetics*, Vol. 45, No. 10, 4526–4529, 2009.

[5] Liu, X., K. T. Chau, J. Z. Jiang, and C. Yu, "Design and analysis of interior-magnet outer-rotor concentric magnetic gears," *Journal of Applied Physics*, Vol. 105, No. 7, 07F101, 2009.

[6] Uppalapati, K. K., M. D. Calvin, J. D. Wright, J. Pitchard, W. B. Williams, and J. Z. Bird, "A magnetic gearbox with an active region torque density of 239 N·m/L," *IEEE Transactions on Industry Applications*, Vol. 54, No. 2, 1331–1338, 2018.

[7] Baninajar, H., S. Modaresahmadi, H. Y. Wong, J. Bird, W. Williams, and B. Dechant, "Designing a halbach rotor magnetic gear for a marine hydrokinetic generator," *IEEE Transactions on Industry Applications*, Vol. 58, No. 5, 6069–6080, 2022.

[8] Mezani, S., K. Atallah, and D. Howe, "A high-performance axial-field magnetic gear," *Journal of Applied Physics*, Vol. 99, No. 8, 08R303, 2006.

[9] Acharya, V. M., J. Z. Bird, and M. Calvin, "A flux focusing axial magnetic gear," *IEEE Transactions on Magnetics*, Vol. 49, No. 7, 4092–4095, 2013.

[10] Bahrami Kouhshahi, M., V. M. Acharya, M. Calvin, J. Z. Bird, and W. Williams, "Designing and experimentally testing a flux-focusing axial flux magnetic gear for an ocean generator appli-

cation," *IET Electric Power Applications*, Vol. 13, No. 8, 1212–1218, 2019.

[11] Davey, K., L. McDonald, and T. Hutson, "Axial flux cycloidal magnetic gears," *IEEE Transactions on Magnetics*, Vol. 50, No. 4, 1–7, 2013.

[12] Jing, L., Y. Wang, D. Li, and R. Qu, "Characteristic analysis of a new structure eccentric harmonic magnetic gear," in *Actuators*, Vol. 12, No. 6, 248, 2023.

[13] Johnson, M., M. C. Gardner, H. A. Toliyat, S. Englebretson, W. Ouyang, and C. Tschida, "Design, construction, and analysis of a large-scale inner stator radial flux magnetically geared generator for wave energy conversion," *IEEE Transactions on Industry Applications*, Vol. 54, No. 4, 3305–3314, 2018.

[14] McGilton, B., R. Crozier, A. McDonald, and M. Mueller, "Review of magnetic gear technologies and their applications in marine energy," *IET Renewable Power Generation*, Vol. 12, No. 2, 174–181, 2018.

[15] Tallerico, T. F., J. J. Scheidler, and Z. A. Cameron, "Electromagnetic mass and efficiency of magnetic gears for electrified aircraft," in *2019 AIAA/IEEE Electric Aircraft Technologies Symposium (EATS)*, 1–25, Indianapolis, IN, USA, 2019.

[16] Wu, Y.-C., F.-M. Ou, M.-C. Tsai, and S. N. Fajri, "Development of a dual-input magnetic gear train for the transmission system of small-scale wind turbines," *Applied Sciences*, Vol. 12, No. 7, 3685, 2022.

[17] Dimauro, L., E. Bonisoli, M. Velardocchia, M. Repetto, P. Alotto, M. Filippini, and R. Torchio, "Magnetic gearbox for automotive power transmissions: An innovative industrial technology," *Engineering Science and Technology, An International Journal*, Vol. 46, 101497, 2023.

[18] Zhu, Z. Q. and D. Howe, "Influence of design parameters on cogging torque in permanent magnet machines," *IEEE Transactions on Energy Conversion*, Vol. 15, No. 4, 407–412, 2000.

[19] Niguchi, N. and K. Hirata, "Cogging torque analysis of magnetic gear," *IEEE Transactions on Industrial Electronics*, Vol. 59, No. 5, 2189–2197, 2012.

[20] Rashid, M. K. and A. M. Mohammed, "Elimination of cogging torque and torque ripple in magnetic gear using slicing technique," *Progress In Electromagnetics Research C*, Vol. 125, 179–189, 2022.

[21] Hsiao, C.-Y., S.-N. Yeh, and J.-C. Hwang, "A novel cogging torque simulation method for permanent-magnet synchronous machines," *Energies*, Vol. 4, No. 12, 2166–2179, 2011.